

PHOTOMETRIC PROPERTIES OF LY α EMITTERS AT $Z \approx 4.86$ IN THE COSMOS 2 SQUARE DEGREE FIELD¹

Y. SHIOYA,² Y. TANIGUCHI,² S. S. SASAKI,^{3, 4} T. NAGAO,^{2, 3} T. MURAYAMA,⁴ T. SAITO,² Y. IDEUE,³ A. NAKAJIMA,³ K. L. MATSUOKA,³ J. TRUMP,^{2, 5} N. Z. SCOVILLE,⁶ D. B. SANDERS,⁷ B. MOBASHER,⁸ H. AUSSEL,⁹ P. CAPAK,^{6, 10} J. KARTALTEPE,⁷ A. KOEKEMOER,¹¹ C. CARILLI,¹² R. S. ELLIS,^{6, 13} B. GARILLI,¹⁴ M. GIAVALISCO,¹¹ M. G. KITZBICHLER,¹⁵ C. IMPEY,⁵ O. LEFEVRE,¹⁶ E. SCHINNERER,¹⁷ AND V. SMOLCIC^{18, 19}

Draft version September 13, 2021

ABSTRACT

We present results of a survey for Ly α emitters at $z \approx 4.86$ based on optical narrowband ($\lambda_c = 7126\text{\AA}$, $\Delta\lambda = 73\text{\AA}$) and broadband (B , V , r' , i' , and z') observations of the Cosmic Evolution Survey (COSMOS) field using Suprime-Cam on the Subaru Telescope. We find 79 LAE candidates at $z \approx 4.86$ over a contiguous survey area of 1.83 deg^2 , down to the Ly α line flux of $1.47 \times 10^{-17} \text{ ergs s}^{-1} \text{ cm}^{-2}$. We obtain the Ly α luminosity function with a best-fit Schechter parameters of $\log L^* = 42.9_{-0.3}^{+0.5} \text{ ergs s}^{-1}$ and $\phi^* = 1.2_{-1.1}^{+8.0} \times 10^{-4} \text{ Mpc}^{-3}$ for $\alpha = -1.5$ (fixed). The two-point correlation function for our LAE sample is $\xi(r) = (r/4.4_{-2.9}^{+5.7} \text{ Mpc})^{-1.90 \pm 0.22}$.

In order to investigate the field-to-field variations of the properties of Ly α emitters, we divide the survey area into nine tiles of $0.5^\circ \times 0.5^\circ$ each. We find that the number density varies with a factor of $\simeq 2$ from field to field with high statistical significance. However, we find no significant field-to-field variance when we divide the field into four tiles with $0.7^\circ \times 0.7^\circ$ each. We conclude that at least 0.5 deg^2 survey area is required to derive averaged properties of LAEs at $z \sim 5$, and our survey field is wide enough to overcome the cosmic variance.

Subject headings: galaxies: distances and redshifts — galaxies: evolution — galaxies: luminosity function, mass function

1. INTRODUCTION

Study of the formation and evolution of galaxies is among the most important topics in modern astro-

physics. An essential component of such investigations is the identification of galaxies at the highest redshifts, when most of the galaxies formed, and study of their rest-frame properties. This requires multi-waveband, wide-area and deep surveys of galaxies to provide statistically significant population of these objects. Recently, complementary observations of selected fields by the largest ground-based and space-borne telescopes have made this aim possible by extending this study to $z \sim 7$ and providing statistically large samples of high redshift galaxies with a significant fraction of them confirmed spectroscopically (see Taniguchi 2008 for a recent review).

To summarize, there are two established techniques to search for high- z galaxy candidates. Firstly, the Lyman break method (i.e. also called drop-out technique) which identifies the continuum break characteristic of Lyman alpha absorption by the Inter-Galactic Medium (IGM) (Steidel et al 1996; for a review see Giavalisco 2002). The high- z candidates selected by this technique are called Lyman break galaxies (LBGs). Secondly, the narrow-band imaging technique which aims for detection of galaxies with strong Lyman α emission- so called Lyman alpha emitters (LAEs) (Taniguchi et al. 2003 for a review). Although both LBGs and LAEs are actively star-forming galaxies, there are systematic differences between them. For example, the stellar populations of LAEs are relatively younger, they have a smaller stellar mass (e.g., Lai et al. 2008), smaller size (e.g., Dow-Hygelund et al. 2007) and are less dusty (e.g, Shapley et al. 2003) compared to the LBGs. These observations imply that the LAEs are likely to be in an earlier star formation phase with respect to LBGs. Furthermore, it is estimated that the average mass of dark matter halos

¹ Based on data collected at Subaru Telescope, which is operated by the National Astronomical Observatory of Japan.

² Research Center for Space and Cosmic Evolution, Ehime University, Bunkyo-cho, Matsuyama 790-8577, Japan

³ Graduate School of Science and Engineering, Ehime University, Bunkyo-cho, Matsuyama 790-8577, Japan

⁴ Astronomical Institute, Graduate School of Science, Tohoku University, Aramaki, Aoba, Sendai 980-8578, Japan

⁵ Steward Observatory, University of Arizona, Tucson, AZ 85721

⁶ Department of Astronomy, MS 105-24, California Institute of Technology, Pasadena, CA 91125

⁷ Institute for Astronomy, University of Hawaii, 2680 Woodlawn Drive, HI 96822

⁸ Department of Physics and Astronomy, University of California, Riverside, CA, 92521

⁹ AIM Unité Mixte de Recherche CEA CNRE Université Paris VII UMR n158 France

¹⁰ Spitzer Science Center, California Institute of Technology, Pasadena, CA 91125

¹¹ Space Telescope Science Institute, 3700 San Martin Drive, Baltimore, MD 21218

¹² National Radio Astronomy Observatory, P.O. Box 0, Socorro, NM 87801-0387

¹³ Department of Astrophysics Keble Road, Oxford OX2 3RH, UK

¹⁴ INAF, Istituto di Astrofisica Spaziale e Fisica Cosmica, Sezione di Milano, via Bassini 15, 20133 Milano, Italy

¹⁵ Max-Planck-Institut für Astrophysik, D-85748 Garching bei München, Germany

¹⁶ Laboratoire d'Astrophysique de Marseille, BP 8, Traverse du Siphon, 13376 Marseille Cedex 12, France

¹⁷ Max Planck Institut für Astronomie, Königstuhl 17, Heidelberg, D-69117, Germany

¹⁸ Princeton University Observatory, Princeton, NJ 08544

¹⁹ University of Zagreb, Department of Physics, Bijenicka cesta 32, 10000 Zagreb, Croatia

hosting LAEs and LBGs at $z \sim 4 - 5$ ($\sim 10^{12} M_{\odot}$) are comparable (Ouchi et al. 2004; Kovač et al. 2007), while, at $z \sim 3.1$ ($\sim 10^{11} M_{\odot}$), it is smaller for the LAEs (Gawiser et al. 2007). This implies that the LAEs at $z \sim 3.1$ are likely progenitors of present-day L^* galaxies, whereas the LAEs at $z \sim 4 - 5$ and LBGs at $z \sim 3 - 5$ will evolve into present-day galaxies with $L > 2.5L^*$ (Gawiser et al. 2007).

To understand differences between the LAEs and LBGs at any given redshift and their properties with look-back time, one needs statistically large and complete samples of these galaxies at different redshifts. Specially for the LAEs, due to technical difficulties in performing narrow-band observations, the majority of these surveys are performed over small areas and in selected redshift slices where there are windows to avoid absorption of the lines by the atmosphere. This problem is particularly serious for candidates at higher redshifts where one needs both depth and wide-area coverage to have sufficient number of galaxies and to minimize the cosmic variance.

For the LAEs at $z \sim 5.7$, extensive studies in different fields have been performed, including: survey around quasar SDSS J1044-0125 (Ajiki et al. 2003), SSA22 (Hu et al. 2004), GOODS-N and GOODS-S (Ajiki et al. 2006), the Subaru Deep Field (SDF) (Shimasaku et al. 2006), the Subaru-XMM Newton Deep Field (SXDF) (Ouchi et al. 2005, 2008) and the Cosmic Evolution Survey (COSMOS) (Murayama et al. 2007). However, there are only limited surveys of LAEs at other redshifts. This is a serious deficiency in studying evolution of clustering of the LAEs and their rest-frame properties specially if these are expected to evolve to nearby elliptical galaxies (Gawiser et al. 2007).

In this paper we perform the largest survey of the LAEs at $z \approx 4.86$, covering the entire 2 square degree of the COSMOS field (Scoville et al. 2007). Earlier studies of the LAEs at this redshift revealed presence of large scale structures of 20×50 Mpc size (Ouchi et al. 2003; Shimasaku et al. 2003), that are comparable to almost the size of the surveyed area, indicating serious cosmic variance in these data (Shimasaku et al. 2003). The survey performed in this study covers an area of $190 \text{ Mpc} \times 190 \text{ Mpc}$ [7 times larger than the survey area of Shimasaku et al. (2003, 2004)], large enough to encompass structures of $\sim 50 \times 50 \text{ Mpc}^2$ size, allowing for proper sampling of the average properties of LAEs at $z \sim 4.9$. Therefore, we are able to examine how the cosmic variance affects the derivation of both the Ly α luminosity functions and the clustering properties for the first time.

In the next section we present our sample selection of LAEs. In section 3 we discuss the Ly α luminosity function and the clustering properties of our sample. We summarize our results in section 4. Throughout this paper, magnitudes are given in the AB system. We adopt a flat universe with $\Omega_{\text{matter}} = 0.3$, $\Omega_{\Lambda} = 0.7$, and $H_0 = 70 \text{ km s}^{-1} \text{ Mpc}^{-1}$.

2. THE SAMPLE

2.1. The Data

We carried out an optical narrow-band (NB711; $\lambda_c = 7126 \text{ \AA}$, $\Delta\lambda = 73 \text{ \AA}$) imaging survey of the entire 2-deg² area of the COSMOS field, using the Suprime-Cam on the Subaru Telescope. The NB711 observations were

done on February 2006 (Taniguchi et al. 2008). The data were reduced using the IMCAT software.²⁰ Combining the NB711 data with the broad-band (B , V , r' , i' , and z') Suprime-Cam imaging data and i^* -band Mega-Prime/CFHT imaging data already available (Taniguchi et al. 2007; Capek et al. 2007),²¹ we identified LAE candidates at $z \approx 4.86$. Details of the narrow-band and broad-band observations and data reduction are presented by Taniguchi et al. (2007, 2008) and Capak et al. (2007).

The FWHMs corresponding to the PSFs on the final images are $0''.95$ (B), $1''.33$ (V), $1''.05$ (r'), $0''.95$ (i'), $1''.15$ (z') and $0''.79$ (NB711). The images were all degraded to a PSF size of $1''.33$. The limiting AB magnitudes of the final PSF matched images are: $B = 27.56$, $V = 26.77$, $r' = 26.95$, $i' = 26.49$, $z' = 25.45$, and NB711 = 25.17 for a 3σ detection in a $3''$ diameter aperture. We then performed source detection on the original NB711 image using SExtractor (Bertin & Arnouts 1996), followed by photometry over an aperture of $3''$ diameter as described in Capak et al (2007). Similarly, i^* band (CFHT) magnitudes over the same aperture, are used to identify interlopers consisting of bright galaxies with $i' < 22$.

After subtracting the masked-out regions, the effective survey area is 1.83 deg^2 . The redshift coverage of NB711 is $4.83 \leq z \leq 4.89$ ($\Delta z = 0.06$), giving an effective survey volume of $1.1 \times 10^6 \text{ Mpc}^3$ (comoving).

2.2. Selection of Lyman α Emitters at $z \approx 4.86$

In order to select NB711-excess objects efficiently, we first need the magnitude of a frequency-matched continuum. Since the effective frequency of the NB711 filter (421.1 THz) lies between r' (482.8 THz) and i' (394.0 THz) bands, we estimate the frequency-matched continuum, “ ri continuum”, using the linear combination: $f_{ri} = 0.3f_{r'} + 0.7f_{i'}$, where $f_{r'}$ and $f_{i'}$ are the flux densities in r' and i' bands respectively. This gives a 3σ limiting magnitude of $ri_{\text{lim},3\sigma} = 26.84$ for the continuum (in a $3''$ diameter aperture). Since brighter objects with $i' < 22$ are saturated in Subaru images, we use the i^* flux density, f_{i^*} , to calculate the “ ri continuum” for such objects, i.e., $f_{ri} = 0.3f_{r'} + 0.7f_{i^*}$.

The NB711-excess objects are then selected using the following criteria:

$$ri - NB711 > 0.7, \quad \text{and} \quad (1)$$

$$ri - NB711 > 3\sigma(ri - NB711), \quad (2)$$

where $3\sigma(ri - NB711) = -2.5 \log \left(1 - \sqrt{(f_{3\sigma_{NB711}})^2 + (f_{3\sigma_{ri}})^2} / f_{NB711} \right)$.

The first criterion corresponding to an observed equivalent width of $EW_{\text{obs}} > 66 \text{ \AA}$, means the flux density in narrow band is twice as large as the flux density of ri continuum. This kind of criterion is conventionally used for LAE survey (e.g., Ouchi et al. 2003; Ajiki et al. 2006; Murayama et al. 2007) to select reliable emitter candidates. Taking account the scatter of the $ri - NB711$ color, we added the second criterion. These two criteria are shown in Figure 1. For objects with

²⁰ IMCAT is distributed by Nick Kaiser at <http://www.ifa.hawaii.edu/~kaiser/imcat/>.

²¹ <http://irsa.ipac.caltech.edu/data/COSMOS/>

$ri < ri_{\text{lim},3\sigma}$, we use the lower-limit value of the *NB711*-excess, $(ri - \text{NB711})_{\text{low.limit}} = ri_{\text{lim},3\sigma} - \text{NB711}$, for our sample selection. We finally select the *NB711*-excess objects with $\text{NB711} < 24.9$.

Following the above criteria, we find a total of 1154 *NB711*-excess objects. These objects includes not only LAEs at $z \approx 4.86$, but other low- z interlopers such as H α , [OIII], and [OII] emitting galaxies. In order to distinguish LAEs from low- z interlopers, we compare the observed broad-band colors of the LAE candidates with colors that are estimated by using the model spectral energy distribution derived by Coleman, Wu, & Weedman (1980), Kinney et al. (1996), and Bruzual & Charlot (2003). Figure 2 shows the $ri - \text{NB711}$ vs. $r' - i'$ color-color diagram with the predicted colors overlaid. Because of the cosmic transmission (Madau et al. 1996), the $r' - i'$ colors of LAEs are predicted to be redder than low- z emission-line galaxies. Based on results from Figure 2, we added another condition to the selection criteria:

$$r' - i' > 0.8. \quad (3)$$

Since the Lyman break is redshifted to $\sim 5300 \text{ \AA}$, the B -band flux of LAEs at $z \approx 4.86$ is expected to be zero. The B -dropout is an effective criterion to distinguish LAEs from low- z interlopers. Here, we must pay attention to the contamination from nearby objects on the sky. If there are objects detected in B -band near the LAE and the fluxes from these objects in the aperture are not negligible, the LAE may be misclassified as a low- z interloper. We show B -band images of two of our final LAE candidates in Figure 3. Although there is no object at the position of the emission-line object (center), the B -band magnitude in $3''$ diameter aperture is brighter than 27.56 (3σ), because of the contamination from the object that lie at a distance of $\sim 1.5''$ from the center. To avoid the contamination from such nearby objects, we adopt the B -band magnitude measured with in the small aperture ($0''.5\phi$) in the original image. We therefore add another selection criterion,

$$B_{\text{original}}(0''.5\phi) > 30.09, \quad (4)$$

where $B_{\text{original}}(0''.5\phi)$ is the B -band magnitude over a $0''.5$ diameter aperture, measured in the original image (i.e. the image before convolving and with a PSF size of $0''.95$). The 3σ limiting magnitude for a $0''.5\phi$ aperture in the original image is 30.09.

Based on the added criteria, we can now clearly distinguish LAEs from the low- z interlopers. We finally select a total of 79 LAE candidates at $z \sim 4.86$. The photometric properties of these LAE candidates are listed in Table 1. Their broad- and *NB711*-band images are presented in Figure 3.

To further check the validity of our photometric selection and their expected redshifts, we extract information of the LAE candidates from the COSMOS spectroscopic catalogue. A total of 7 LAEs in our final candidate list have spectroscopic redshifts. Figure 4 presents the spectroscopic redshift distribution of these LAEs. This peaks at $z \approx 4.85$ with all the spectroscopic redshifts lying in the range $4.80 < z < 4.85$. This result suggests that our selection criteria works quite well to identify LAEs at $z \approx 4.9$.

2.3. Ly α Luminosity

We estimate the line fluxes for our LAE candidates, F_L , using the prescription by Pascual et al. (2001). We express the flux density in each filter band using the line flux, F_L , and the continuum flux density, f_C :

$$f_{\text{NB}} = f_C + \frac{F_L}{\Delta \text{NB}} \quad (5)$$

$$f_{r'} = f_C \quad (6)$$

$$f_{i'} = f_C + \frac{F_L}{\Delta i'}, \quad (7)$$

where ΔNB and $\Delta i'$ are the effective bandwidths of *NB711* and i' , respectively. The ri continuum is expressed as

$$f_{ri} = 0.3f_{r'} + 0.7f_{i'} = f_C + 0.7\frac{F_L}{\Delta i'}. \quad (8)$$

Using equations (5) and (8), the line flux, F_L , is calculated by

$$F_L = \Delta \text{NB} \frac{f_{\text{NB}} - f_{ri}}{1 - 0.7(\Delta \text{NB}/\Delta i')}. \quad (9)$$

The limiting line flux of our survey is $1.47 \times 10^{-17} \text{ ergs s}^{-1}$. Since the response curve is not square in shape, the observed flux of Ly α emission for a fixed Ly α luminosity depends on the redshift. On average, the observed flux is underestimated by a factor of 0.81, which is calculated by

$$\frac{\int_{\lambda_c - \Delta\lambda/2}^{\lambda_c + \Delta\lambda/2} R(\lambda) d\lambda}{\int_{\lambda_c - \Delta\lambda/2}^{\lambda_c + \Delta\lambda/2} d\lambda} = 0.81,$$

where $R(\lambda)$ is a response function normalized by the maximum value. We therefore apply correction statistically for the filter response by $F_{\text{cor}}(\text{Ly}\alpha) = F_L \times 1.24$. Finally, we estimate the Ly α luminosity as $L(\text{Ly}\alpha) = 4\pi d_L^2 F_{\text{cor}}(\text{Ly}\alpha)$. In this procedure, we assume that all the LAEs are located at $z = 4.86$ ($d_L = 45.1 \text{ Gpc}$), the redshift corresponding to the central wavelength of our *NB711* filter.

3. RESULTS AND DISCUSSION

3.1. Spatial Distribution

Figure 6 presents the spatial distribution of our 79 LAE candidates at $z \sim 4.86$. The contours of local surface density ($2\bar{\Sigma}$, where $\bar{\Sigma}$ is the averaged surface density over the whole field, 43 degree^{-2}) are shown in the figure. The local surface density at position (x, y) is the density averaged over the circle centered at (x, y) , whose radius is determined as the angular distance to the 3rd nearest neighbors. There are ten overdensity regions in the field. A typical size of the large overdensity region is $0.4^\circ \times 0.2^\circ$ ($50 \text{ Mpc} \times 25 \text{ Mpc}$), being similar to those found by Shimasaku et al. (2003) and Ouchi et al. (2005).

To check for field-to-field variation, we divide the survey area into nine subfields, each corresponding to a sky area of $0.5^\circ \times 0.5^\circ$ ($63 \text{ Mpc} \times 63 \text{ Mpc}$) (Figure 6). The number density of the LAEs in each subfield is summarized in Table 2. We find significant field-to-field variations among the nine subfields by a factor of $\simeq 2$. This means that the typical scale of the large scale structure

is comparable to the size of the subfield, that is consistent with the size of the overdensity regions found in the above. The field-to-field variations found here, agrees with those for LAEs at $z \approx 5.7$, independently estimated in the SXDF (Ouchi et al. 2008) and with theoretical predictions using the cosmological hydrodynamic simulations (Nagamine et al. 2008) for the fields of $\sim 0.2 \text{ deg}^2$. Our finding suggests that the derived properties of LAEs from the survey with a small survey area (smaller than $0.5^\circ \times 0.5^\circ$) may be affected by the cosmic variance.

We also divide the survey area into four subfields, each corresponding to a sky area of $0.7^\circ \times 0.7^\circ$ ($95 \text{ Mpc} \times 95 \text{ Mpc}$). We find 21, 21, 19 and 18 LAEs in NE, NW, SW, and SE quadrant, respectively. This means that the typical scale of the large scale structure is smaller than the size of the subfield. Our finding suggests that the derived properties of LAEs from the survey with a large survey area (larger than $0.7^\circ \times 0.7^\circ$) are considered to be averaged ones over the universe at $z \sim 5$.

3.2. Ly α Luminosity Function

The rest-frame Ly α luminosity function (LF) for our sample of LAEs at $z \approx 4.86$ is presented in Figure 7. The LF is measured as

$$\Phi(\log L_i) = \frac{N_i}{V_{\text{co}}}, \quad (10)$$

where V_{co} is the comoving volume of $1.1 \times 10^6 \text{ Mpc}^3$ ($4.83 \leq z \leq 4.89$) and N_i is a number of LAEs within $\log L_i \pm \frac{1}{2} \Delta \log L$. We use $\Delta \log L(\text{Ly}\alpha) = 0.2$. We fit the rest-frame Ly α LF with the Schechter function (Schechter 1976) using parametric maximum likelihood estimator (Sandage, Tammann, & Yahil 1979). Since the characteristic luminosity (L^*) and the faint-end slope (α) of the Schechter LFs are not independent, we perform the fit by fixing α to -1 , -1.5 , and -2 . Our best-fit Schechter parameters are summarized in Table 3. For comparison, we also plot the Ly α LF for a sample selected by Ouchi et al. (2003). Their survey was performed by using the same narrowband filter (NB711), for smaller field (543 arcmin^2) and deeper (down to $\text{NB711} = 26.0$) than ours. Although our sample does not include low-luminosity LAEs and their sample does not include LAEs at the luminous-end, our Ly α LF is consistent with that of Ouchi et al. (2003) for the range of $42.8 \leq \log L(\text{Ly}\alpha) \leq 43.2$.

Since the filter response curve of NB711 is not box-shaped, the narrow-band magnitude of LAEs of a fixed Ly α luminosity varies as a function of the redshift. The selection function of LAEs in terms of the equivalent width also changes with the redshift (Shimasaku et al. 2006; Ouchi et al. 2008). We check the validity of the Ly α LF derived above. In order to examine whether or not we can reconstruct an input Ly α LF by our selection criteria and an estimation of Ly α flux, we performed the Monte Carlo simulations that are similar to those made by Shimasaku et al. (2006). First, we generate a mock catalog of LAEs with a set of the Schechter parameters (α , ϕ^* , L^*) and a Gaussian distribution function of EW , $f(EW_0)dEW_0 \propto \exp(-EW_0^2/2\sigma_{EW}^2)dEW_0$. We adopt four σ_{EW} values: $\sigma_{EW} = 50, 100, 200$, and 400 \AA . We uniformly distribute them in comoving space over $4.7 < z < 5.1$. Next, we select Ly α emitters and evalu-

ate the Ly α LF applying the method written above for the mock catalog. We show results of our simulations in Figure 8. We confirm that the Ly α LF we evaluate is very close to the input LF. We conclude that the simple method we adopted is valid for evaluating the Ly α LF.

We plot the Ly α LFs from the four subfields in Figure 7 (*left panel*). Those LFs are consistent within their errors. We also summarize the best-fit Schechter parameters for four subfields in Table 4. Although the field-to-field variation of ϕ^* is a factor of 4, each value exist within the error in Table 3. In Figure 7 (*right panel*), we compare our results with other LAE surveys in the redshift range $z \sim 3.1 - 6.6$. Although various surveys have slightly different selection criteria, most of the Ly α LFs are similar to each other. We then find that estimated Ly α LF is very similar to those at $3.1 \leq z \leq 5.7$ within errors. This result supports the little evolution of Ly α LFs in the range of $3 < z < 6$ (Tran et al. 2004; van Breukelen et al. 2005; Shimasaku et al. 2006; Ouchi et al. 2008).

3.3. Equivalent Widths

Figure 9 shows the distribution of $EW_0(\text{Ly}\alpha)$. To measure the rest-frame UV continuum flux, we use the z' -band data as the fluxes at i' -band are affected by Ly α emission. For objects fainter than 1σ in the z' band, we calculate the upper-limit of the UV luminosity, $L_\nu(\text{UV})$, and the lower-limit of the rest-frame equivalent width, $EW_0(\text{Ly}\alpha)$. The $EW_0(\text{Ly}\alpha)$ distribution is similar to those in previous studies of LAEs at $z \sim 3-6$ (e.g., Shimasaku et al. 2006; Dawson et al. 2007; Ouchi et al. 2008; Gronwall et al. 2008), with the mean rest-frame Lyman α equivalent widths of the sample smaller than 200 \AA . There is no LAE with $EW_0(\text{Ly}\alpha) > 250 \text{ \AA}$ in our sample, although the rest-frame Ly α equivalent widths of 23 of the LAEs in our sample (29%) are lower limits. Taking account of a predicted $EW_0(\text{Ly}\alpha)$ for starburst galaxies, 300 \AA for young starburst (age $\leq 10^6 \text{ yr}$) and 100 \AA for old starburst (age $\sim 10^8 \text{ yr}$) (Malhotra & Rhoads 2002), we consider that there is no peculiar object in our sample. Figure 10 shows the relation between $EW_0(\text{Ly}\alpha)$ and M_{UV} . There is no object with $EW_0(\text{Ly}\alpha) > 80 \text{ \AA}$ in the UV-bright ($M_{\text{UV}} < -21.5$) sample. Although the number of UV-bright LAEs is small and the uncertainties on EW_0 s for UV-faint objects are large, this trend is similar to that found for LBGs and LAEs at $z \sim 5-6$ (Ando et al. 2006; Shimasaku et al. 2006; Ouchi et al. 2008). We conclude that our sample shows the ‘‘average’’ picture of bright LAEs at $z \sim 5$.

3.4. UV Luminosity Function

Figure 11 shows UV LF of our sample (black symbols). The UV LFs of LAEs estimated in the four subfields are consistent within errors. Figure 11 also include the UV LF of LBGs at $z \sim 5$ (Yoshida et al. 2006) and LAEs at $z \sim 3.1, 3.7$, and 5.7 (Ouchi et al. 2008). The shape of our UV LF seems different from those of previous works and is not fit by Schechter function, since a detection limit of rest-frame equivalent width, $EW_0(\text{Ly}\alpha)$, depends on M_{UV} , e.g., $EW_0(\text{Ly}\alpha) > 11 \text{ \AA}$ at $M_{\text{UV}} < -21.5$ and $EW_0(\text{Ly}\alpha) > 57 \text{ \AA}$ at $M_{\text{UV}} = -20$ (see Figure 10). As a reference, we overlay the result of our Monte Carlo simulation for $\alpha = -1.5$ and $\sigma_{EW} = 100 \text{ \AA}$: dotted line

show input UV LF for $EW_0(\text{Ly}\alpha) > 11\text{\AA}$ and solid line show output UV LF. This result also shows that our UV LF is considered to be complete for LAE with $EW_0 > 11\text{\AA}$ for $M_{\text{UV}} < -21.5$. We therefore concentrate the number density at $M_{\text{UV}} < -21.5$.

First, we compare our UV LF with that of LBGs at $z \sim 5$. The number density of our LAEs is comparable to that of LBGs at $z \sim 5$ at $M_{\text{UV}} \sim -22$ and ~ 20 –25 % at $M_{\text{UV}} = -21.5$. Ouchi et al. (2008) pointed out that the ratio of number densities of LAEs to those of LBGs is $\sim 10\%$ at $z = 3$ –4 and $> 50\%$ at $z = 5.7$. Our result imply that the ratio of the number density of LAEs to that of LBGs becomes larger with redshift from $z = 4$ to 5. Next, we compare our UV LF with those of LAEs at different redshifts. Figure 12 shows the number density of LAEs at $M_{\text{UV}} = -21.5$ as a function of z . The number density of our LAEs at $M_{\text{UV}} = -21.5$ is comparable to that of LAEs at $z \sim 5.7$, while larger than those of LAEs at $z \sim 3.1$ and 3.7. The number density of UV-bright LAEs ($M_{\text{UV}} < -21.5$) increases an order of magnitude with redshift from $z = 4$ to 5. Since it is likely that the LAEs are star-forming galaxies in an earlier star formation phase, our findings imply that the initial active star-formation phase occur mainly beyond $z = 5$.

3.5. Clustering Properties

We found the large scale structure of LAEs of $0.4^\circ \times 0.2^\circ$ in subsection 3.1. In order to perform a more quantitative study of the clustering properties of the LAEs at $z \sim 4.86$, we derive their angular two-point correlation function (ACF), $w(\theta)$, using the estimator defined by Landy & Szalay (1993),

$$w(\theta) = \frac{DD(\theta) - 2DR(\theta) + RR(\theta)}{RR(\theta)}, \quad (11)$$

where $DD(\theta)$, $DR(\theta)$, and $RR(\theta)$ are normalized numbers of galaxy-galaxy, galaxy-random, and random-random pairs, respectively. The random sample here consists of 100,000 sources with the same geometrical constraints as the galaxy sample. The observed ACF is fit well by a single power law: $w(\theta) = 0.021_{-0.011}^{+0.025} \theta^{-0.90 \pm 0.22}$ (Figure 13). The correlation length, r_0 , is calculated from the ACF through Limber's equation (e.g., Peebles 1980), assuming a top-hat redshift distribution centered on $z = 4.86 \pm 0.03$. We estimated the r_0 corresponding to our sample of LAEs as $r_0 = 4.4_{-2.9}^{+5.7}$ Mpc. The two-point correlation function is thus written as $\xi(r) = (r/4.4_{-2.9}^{+5.7} \text{Mpc})^{-1.90 \pm 0.22}$. This agrees well with results from other works at similar redshifts, e.g., $r_0 = 5.0 \pm 0.4$ for $z \simeq 4.9$ (Ouchi et al. 2003); $r_0 = 4.57 \pm 0.60$ for $z \simeq 4.5$ (Kovač et al. 2007).

Also shown in Figure 13 are the ACFs for the LAEs

in the four subfields. We detect strong clustering signals in small scale ($\theta \leq 50$ arcsec) for NE, SW, and SE subfields, with the NW subfield showing no clustering signals at any angular separations. Although this may imply the presence of a cosmic variance on the clustering properties similar to that found in a previous study (Shimasaku et al. 2004), taking account of large uncertainties of ACFs, we consider that there are no significant field-to-field variations among the four subfields.

4. SUMMARY

We have performed the largest survey to date for Ly α emitters at $z \approx 4.86$, using narrow-band (NB711) imaging technique in the COSMOS 2 square degree field. We have found a total of 79 Ly α emission-line galaxy candidates. For 7 LAE candidates with available spectroscopic data, we have confirmed that our criteria for selecting LAEs at $z \approx 4.86$ are working well. Our results and conclusions are summarized below,

1. We have found a field-to-field variation of the number density of LAEs as large as a factor of $\simeq 2$ among the nine subfields with $0.5^\circ \times 0.5^\circ$. On the other hand, the number density of LAEs for four subfields with $0.7^\circ \times 0.7^\circ$ is consistent within a error. This finding is consistent with the scale of large scale structure we found, 50 Mpc \times 25 Mpc. We conclude that at least 0.5 deg² survey area is required to derive averaged properties of LAEs at $z \sim 5$, and our survey field is wide enough to overcome the cosmic variance.

2. The Ly α LF is well-fitted by a Schechter function with best-fit Schechter parameters: $\log L^* = 42.91_{-0.31}^{+0.49} \text{ergs s}^{-1}$ and $\phi^* = 1.22_{-1.05}^{+8.02} \times 10^{-4} \text{Mpc}^{-3}$ for $\alpha = -1.5$ (fixed). The two-point correlation function is well fitted by a power law, $w(\theta) = 0.021_{-0.011}^{+0.025} \theta^{-0.90 \pm 0.22}$, giving $\xi(r) = (r/4.4_{-2.9}^{+5.7} \text{Mpc})^{-1.9}$.

3. We have derived the UV LF of LAEs. The number density of our LAEs at $M_{\text{UV}} = -21.5$ are similar to those of LAEs at $z \sim 5.7$ while larger than those of LAEs at $z \sim 3$ –4. The number density of UV-bright LAEs increases an order of magnitude with redshift from $z \sim 4$ to $z \sim 5$.

The HST COSMOS Treasury program was supported through NASA grant HST-GO-09822. We greatly acknowledge the contributions of the entire COSMOS collaboration consisting of more than 70 scientists. We would like to thank Masami Ouchi for useful discussion and the anonymous referee for valuable comments. We would also like to thank the Subaru Telescope staff for their invaluable help. This work was financially supported in part by the JSPS (Nos. 15340059 and 17253001).

REFERENCES

- Ajiki, M., Mobasher, B., Taniguchi, Y., Shioya, Y., Nagao, T., Murayama, T., & Sasaki, S. S. 2006, ApJ, 638, 596
 Ajiki, M., et al. 2003, AJ, 126, 2091
 Ando, M., Ohta, K., Iwata, I., Watanabe, C., Tamura, N., Akiyama, M., & Aoki, K. 2004, ApJ, 610, 635
 Ando, M., Ohta, K., Iwata, I., Akiyama, M., Aoki, K., & Tamura, N. 2006, ApJ, 645, L9
 Bertin, E., & Arnouts, S. 1996, A&AS, 117, 393
 Bruzual A., G., & Charlot, S. 2003, MNRAS, 344, 1000
 Capak, P., et al. 2007, ApJS, 172, 99
 Coleman, G. D., Wu, C.-C., & Weedman, D. W. 1980, ApJS, 43, 393
 Cowie, L. L., & Hu, E. M. 1998, AJ, 115, 1319
 Dawson, S., et al. 2007, ApJ, 671, 1227
 Dow-Hygelund, C. C., et al. 2007, ApJ, 660, 47
 Gawiser, E., et al. 2007, ApJ, 671, 278
 Giavalisco, M. 2002, ARA&A, 40, 579
 Gronwall, C., et al. 2007, ApJ, 667, 79

- Hu, E. M., et al. 2004, *AJ*, 127, 563
Kinney et al. 1996, *ApJ*, 467, 38
Kovač, K., Somerville, R. S., Rhoads, J. E., Malhotra, S., & Wang, J. 2007, *ApJ*, 668, 15
Lai, K. et al. 2008, *ApJ*, 674, 70
Landy, S. D., Szalay, A. S. 1993, *ApJ*, 412, 64
Madau, P., Ferguson, H. C., Dickinson, M. E., Giavalisco, M., Steidel, C. C., & Fruchter, A. 1996, *MNRAS*, 283, 1388
Malhotra, S., & Rhoads, J. E. 2002, *ApJ*, 565, L71
Murayama, T., et al. 2007, *ApJS*, 172, 523
Nagamine, K., Ouchi, M., Springel, V., & Hernquist, L. 2008, preprint (arXiv:0802.0228)
Ouchi, M., et al. 2003, *ApJ*, 582, 60
Ouchi, M., et al. 2004, *ApJ*, 611, 685
Ouchi, M., et al. 2005, *ApJ*, 620, L1
Ouchi, M., et al. 2008, *ApJS*, 176, 301
Pascual, S., Gallego, J., Aragón-Salamanca, A., & Zamorano, J. 2001, *A&A*, 379, 798
Peebles, P. J. E. 1980, *The Large-Scale Structure of the Universe* (Princeton: Princeton Univ. Press)
Sandage, A., Tammann, G. A., & Yahil, A. 1979, *ApJ*, 232, 352
Schechter, P. 1976, *ApJ*, 203, 297
Scoville, N., et al. 2007, *ApJS*, 172, 1
Shapley, A. E., Steidel, C. C., Pettini, M., & Adelberger, K. L. 2003, *ApJ*, 588, 65
Shimasaku, K., et al. 2003, *ApJ*, 586, L111
Shimasaku, K., et al. 2004, *ApJ*, 605, L93
Shimasaku, K., et al. 2006, *PASJ*, 58, 313
Taniguchi, Y. 2008, in *IAU Symp. 250, Massive Stars as Cosmic Engine*, ed. F. Bresolin, P. Crowther, & J. Puls, (Cambridge: Cambridge Univ. Press), in press (arXiv:0804.0644)
Taniguchi, Y., et al. 2003, *JKAS*, 36, 123; Erratum 36, 283
Taniguchi, Y., et al. 2005, *PASJ*, 57, 165
Taniguchi, Y., et al. 2007, *ApJS*, 172, 9
Taniguchi, Y., et al. 2008, in preparation
Tran, K.-V. H., Lilly, S. J., Crampton, D., & Brodwin, M. 2004, *ApJ*, 612, L89
van Breukelen, C., Jarvis, M. J., & Venemans, B. P. 2005, *MNRAS*, 359, 895
Yoshida, M., et al. 2006, *ApJ*, 653, 988

TABLE 1
A LIST OF Ly α EMITTER CANDIDATES.

#	RA (deg)	DEC (deg)	r' (mag)	i' (mag)	ri (mag)	$NB711$ (mag)	z' (mag)	$\log L(\text{Ly}\alpha)$ (ergs s $^{-1}$)	$\log L_\nu(1540\text{\AA})$ (ergs s $^{-1}$ Hz $^{-1}$)	M_{UV} (mag)	EW_0 (\AA)
1	150.68983	1.598039	28.85	26.54	26.87	24.86	25.95	42.68	28.80	-20.4	46
2	150.58466	1.528353	26.26	25.13	25.36	23.52	25.40	43.20	29.02	-21.0	90
3	150.43377	1.584748	27.49	26.38	26.61	24.46	> 26.64	42.85	< 28.52	> -19.7	> 127
4	150.47017	1.527121	27.85	26.69	26.92	24.76	26.28	42.73	28.67	-20.1	69
5	150.12679	1.606008	27.15	25.63	25.91	23.43	25.61	43.28	28.94	-20.7	131
6	150.19137	1.514911	25.95	25.13	25.32	24.47	24.79	42.64	29.26	-21.6	14
7	149.42627	1.570369	27.34	25.94	26.21	24.44	> 26.64	42.83	< 28.52	> -19.7	> 121
8	149.50750	1.569846	26.40	24.72	25.01	24.05	25.06	42.85	29.15	-21.3	30
9	150.72870	1.654431	27.26	26.02	26.27	24.22	> 26.64	42.94	< 28.52	> -19.7	> 156
10	150.69867	1.658967	99.00	27.04	27.42	24.80	> 26.64	42.74	< 28.52	> -19.7	> 98
11	150.69845	1.643227	27.19	25.73	26.00	24.55	24.98	42.75	29.19	-21.4	22
12	150.44771	1.639259	26.33	24.16	24.48	23.64	24.31	42.98	29.46	-22.0	20
13	150.21979	1.647579	27.64	25.97	26.26	24.71	25.67	42.70	28.91	-20.7	36
14	149.92387	1.706955	27.91	26.99	27.19	24.22	> 26.64	42.98	< 28.52	> -19.7	> 171
15	149.86911	1.741172	27.83	25.18	25.52	24.07	25.43	42.94	29.01	-20.9	51
16	149.81740	1.738043	26.33	25.43	25.63	24.46	25.87	42.73	28.83	-20.5	47
17	149.85339	1.702846	28.17	26.76	27.03	24.74	> 26.64	42.75	< 28.52	> -19.7	> 100
18	149.81761	1.638761	26.26	25.23	25.45	24.10	25.25	42.91	29.08	-21.1	41
19	149.47913	1.713145	26.26	24.90	25.17	24.18	24.82	42.81	29.25	-21.5	21
20	150.77783	1.795379	27.63	25.85	26.15	24.38	25.44	42.85	29.00	-20.9	42
21	150.43713	1.821238	27.16	25.26	25.57	23.96	24.83	43.00	29.25	-21.5	34
22	150.39265	1.852772	30.47	26.36	26.74	24.51	> 26.64	42.84	< 28.52	> -19.7	> 122
23	150.31602	1.848847	26.35	24.94	25.21	24.41	24.73	42.65	29.29	-21.6	14
24	149.98396	1.914333	27.61	26.12	26.39	24.49	> 26.64	42.82	< 28.52	> -19.7	> 119
25	149.76505	1.835950	26.46	25.04	25.31	24.38	24.49	42.71	29.38	-21.9	13
26	149.82192	1.826156	27.56	26.12	26.39	24.46	> 26.64	42.83	< 28.52	> -19.7	> 122
27	149.70144	1.880336	29.66	25.88	26.26	24.38	25.73	42.86	28.89	-20.6	56
28	149.43575	1.958916	25.53	24.38	24.62	23.34	24.16	43.20	29.51	-22.2	29
29	150.52280	2.053999	28.66	26.82	27.13	23.87	> 26.64	43.13	< 28.52	> -19.7	> 240
30	150.44155	2.045647	25.92	24.17	24.47	23.50	24.13	43.07	29.53	-22.2	21
31	149.80258	1.976421	28.37	26.13	26.46	24.58	25.48	42.78	28.99	-20.9	37
32	149.47068	2.112708	28.53	27.11	27.38	24.84	> 26.64	42.72	< 28.52	> -19.7	> 94
33	149.49438	2.111401	27.52	26.13	26.39	24.64	> 26.64	42.75	< 28.52	> -19.7	> 100
34	149.50653	2.059920	26.21	24.78	25.05	23.56	25.14	43.15	29.12	-21.2	63
35	149.42625	1.971732	27.00	25.60	25.87	23.59	25.36	43.21	29.04	-21.0	89
36	150.75362	2.237688	27.53	26.18	26.45	24.37	26.27	42.88	28.67	-20.1	97
37	150.74435	2.216502	25.70	24.59	24.82	24.08	24.31	42.76	29.45	-22.0	12
38	150.23097	2.219221	27.93	26.37	26.65	24.04	> 26.64	43.04	< 28.52	> -19.7	> 196
39	150.17687	2.162903	27.02	26.05	26.26	24.21	> 26.64	42.95	< 28.52	> -19.7	> 157
40	149.96795	2.258172	27.64	26.05	26.34	24.76	26.26	42.68	28.68	-20.1	60
41	150.01739	2.146056	26.51	24.88	25.17	23.39	25.62	43.25	28.93	-20.7	124
42	149.83435	2.270296	26.92	25.37	25.65	23.82	25.58	43.08	28.95	-20.8	81
43	150.68548	2.422582	26.74	25.83	26.03	24.49	25.59	42.78	28.94	-20.8	41
44	150.48986	2.405317	26.14	24.93	25.17	23.91	25.16	42.97	29.11	-21.2	43
45	150.34351	2.380535	26.92	26.01	26.22	24.62	26.54	42.74	28.56	-19.8	89
46	150.17116	2.443712	27.53	25.48	25.79	24.65	25.27	42.66	29.07	-21.1	23
47	149.95843	2.414291	29.20	26.60	26.95	24.70	26.49	42.76	28.58	-19.9	89
48	149.86004	2.390346	27.06	26.09	26.31	23.95	> 26.64	43.07	< 28.52	> -19.7	> 208
49	149.62681	2.428601	31.96	26.72	27.11	24.93	25.84	42.66	28.84	-20.5	40
50	149.51027	2.301385	27.33	26.22	26.45	23.69	26.34	43.19	28.64	-20.0	208
51	150.72903	2.584166	26.45	25.56	25.76	24.64	25.67	42.65	28.91	-20.7	33
52	150.78495	2.573355	26.58	25.42	25.66	24.62	25.31	42.64	29.06	-21.0	23
53	150.75115	2.481606	28.43	26.25	26.57	24.41	> 26.64	42.87	< 28.52	> -19.7	> 133
54	150.24314	2.530345	27.07	25.42	25.71	23.45	25.44	43.26	29.00	-20.9	108
55	150.13505	2.486044	26.83	25.21	25.50	24.50	25.22	42.68	29.09	-21.1	23
56	149.89657	2.527743	26.57	25.42	25.66	24.45	26.08	42.75	28.75	-20.3	59
57	149.75765	2.572967	28.44	26.53	26.84	24.67	25.54	42.77	28.96	-20.8	38
58	149.87223	2.497300	27.31	25.72	26.00	23.90	25.50	43.07	28.98	-20.9	74
59	149.60335	2.612591	26.85	25.52	25.78	24.52	26.03	42.73	28.77	-20.3	55
60	149.58816	2.521003	27.14	25.43	25.73	24.14	25.28	42.93	29.07	-21.1	43
61	149.46094	2.563734	27.24	26.09	26.33	24.80	25.71	42.66	28.90	-20.6	35
62	150.80329	2.730062	26.73	25.50	25.75	24.59	25.90	42.68	28.82	-20.5	43
63	150.76442	2.688660	25.39	24.31	24.53	23.68	23.91	42.96	29.62	-22.4	13
64	150.43973	2.720629	26.24	25.09	25.33	24.27	25.30	42.78	29.06	-21.1	32
65	150.30282	2.772591	26.65	25.06	25.34	24.41	24.81	42.70	29.26	-21.5	16
66	150.30023	2.666173	28.11	26.84	27.09	24.88	> 26.64	42.69	< 28.52	> -19.7	> 87
67	150.28152	2.651694	27.53	26.16	26.42	24.16	> 26.64	42.98	< 28.52	> -19.7	> 170
68	150.29721	2.634812	26.25	24.65	24.94	24.06	25.12	42.82	29.13	-21.2	29
69	149.94445	2.704370	26.02	25.20	25.39	24.49	25.79	42.66	28.86	-20.6	37
70	149.78731	2.678302	26.12	24.67	24.94	23.50	24.88	43.16	29.23	-21.5	52
71	149.66107	2.739789	26.23	24.87	25.14	24.32	24.66	42.69	29.31	-21.7	14
72	149.72632	2.664706	99.00	25.59	25.98	24.35	> 26.64	42.85	< 28.52	> -19.7	> 126
73	149.43064	2.784033	28.95	26.30	26.65	24.81	> 26.64	42.69	< 28.52	> -19.7	> 87
74	149.41782	2.735198	26.83	25.45	25.71	24.41	> 26.64	42.78	< 28.52	> -19.7	> 107
75	149.44796	2.694757	26.55	25.36	25.60	24.54	24.89	42.68	29.22	-21.5	17
76	150.31928	2.864155	27.78	26.37	26.64	24.66	> 26.64	42.76	< 28.52	> -19.7	> 102
77	150.23253	2.849228	99.00	26.19	26.58	24.70	> 26.64	42.74	< 28.52	> -19.7	> 97
78	149.80660	2.861745	25.88	25.05	25.24	23.25	24.83	43.33	29.25	-21.5	71
79	149.43851	2.902153	26.54	25.58	25.79	24.62	25.48	42.67	28.99	-20.9	29

TABLE 2
THE NUMBER DENSITY OF LAES IN THE 9
SUBFIELDS OF $0.5^\circ \times 0.5^\circ$.

	East (deg ⁻²)	Middle (deg ⁻²)	West (deg ⁻²)
North	29.6 ± 12.1	52.0 ± 15.7	64.3 ± 17.8
Middle	30.9 ± 12.6	28.0 ± 11.4	45.3 ± 15.1
South	59.5 ± 17.9	28.0 ± 11.4	53.1 ± 16.0

TABLE 3
BEST-FIT SCHECHTER PARAMETERS FOR
LY α LUMINOSITY FUNCTIONS.

α (fixed)	$\log L_{\text{Ly}\alpha}^*$ (erg s ⁻¹)	ϕ^* ($\times 10^{-4}$ Mpc ⁻³)
-1.0	42.82 ^{+0.39} _{-0.28}	1.41 ^{+6.73} _{-1.09}
-1.5	42.91 ^{+0.49} _{-0.31}	1.22 ^{+8.02} _{-1.05}
-2.0	43.00 ^{+0.70} _{-0.37}	0.82 ^{+9.98} _{-0.77}

TABLE 4
BEST-FIT SCHECHTER PARAMETERS FOR LY α
LUMINOSITY FUNCTIONS FOR EACH SUBFIELD.

α (fixed)	subfield	$\log L_{\text{Ly}\alpha}^*$ (erg s ⁻¹)	ϕ^* ($\times 10^{-4}$ Mpc ⁻³)
-1.0	NE	42.79	0.85
	NW	42.76	3.0
	SW	42.92	0.84
	SE	42.83	1.4
-1.5	NE	42.87	0.78
	NW	42.84	2.7
	SW	43.02	0.68
	SE	42.91	1.2
-2.0	NE	42.97	0.56
	NW	42.94	2.0
	SW	43.15	0.40
	SE	43.02	0.83

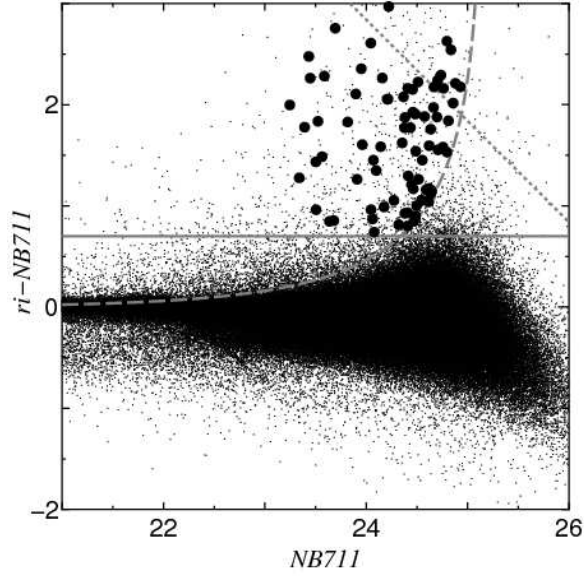


FIG. 1.— $ri - NB711$ vs. $NB711$ diagram for all the $NB711$ detected sources in COSMOS. The horizontal solid line corresponds to $ri - NB711 = 0.7$. The dashed line show the distribution of the 3σ errors. The dotted line shows the limiting magnitude of ri . Filled circles represent 79 LAE candidates detected here.

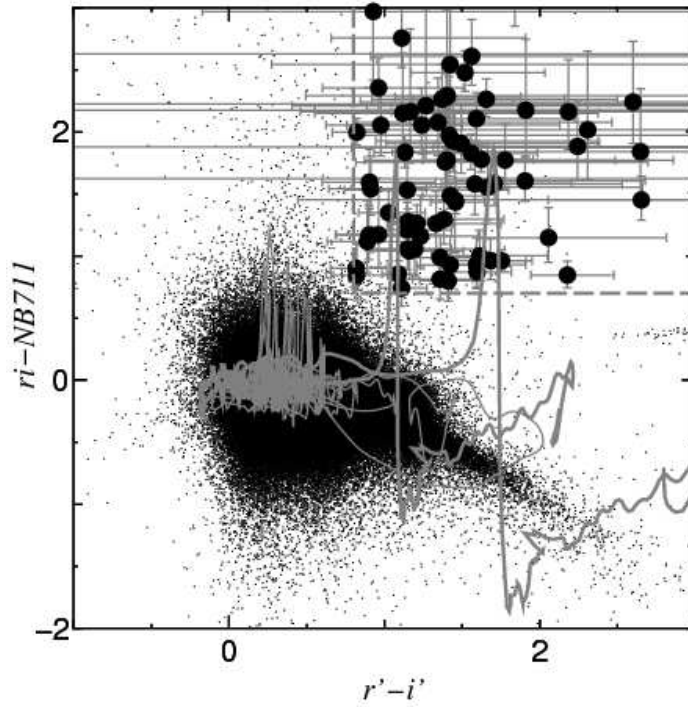


FIG. 2.— $ri - NB711$ vs. $r' - i'$ diagram. Thick gray lines show colors of model LAE SEDs, which are calculated with BC03 model (Bruzual & Charlot 2003) with an exponential decay time of $\tau = 1$ Gyr and an age of 1 Gyr, corresponding to a cosmic transmission of $0.5\tau_{\text{eff}}$ (left) and τ_{eff} (right) in the formulation of Madau et al. (1996). Luminosity of the $\text{Ly}\alpha$ emission is calculated as $L(\text{Ly}\alpha) = 1.2 \times 10^{-11} N_{\text{Ly}\alpha}$, where $N_{\text{Ly}\alpha}$ is the ionizing photon production rate (Leitherer & Heckman 1995; Brocklhurst 1971). Thin gray lines show color loci of starburst galaxies (Kinney et al. 1996), typical elliptical, spiral, and irregular galaxies (Coleman, Wu, & Weedman 1980) up to $z = 2$.

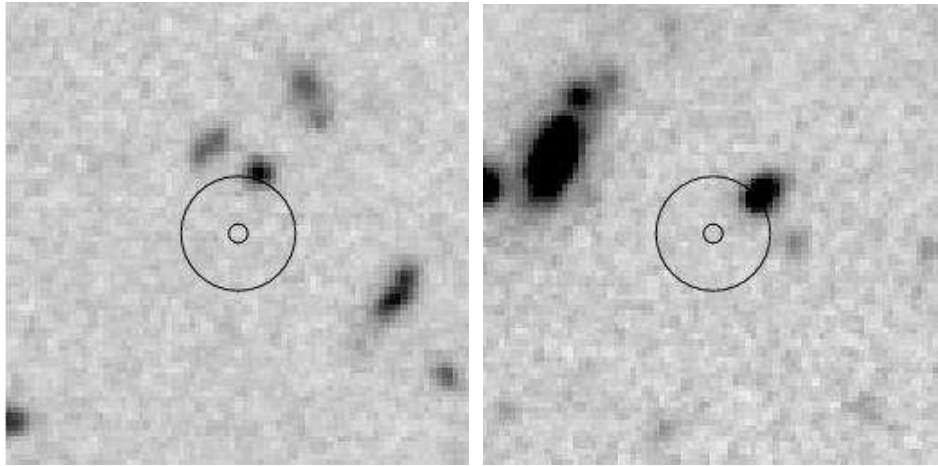


FIG. 3.— *B*-band images of our LAE candidates #16 & #44. Each box is $12''$ on a side (north is up and east is left). The diameter of a small (large) circle is $0''.5$ ($3''$). In both cases, there are no counter part in the center, although the flux within $3''$ diameter aperture is larger than 3σ because of the contamination from nearby objects.

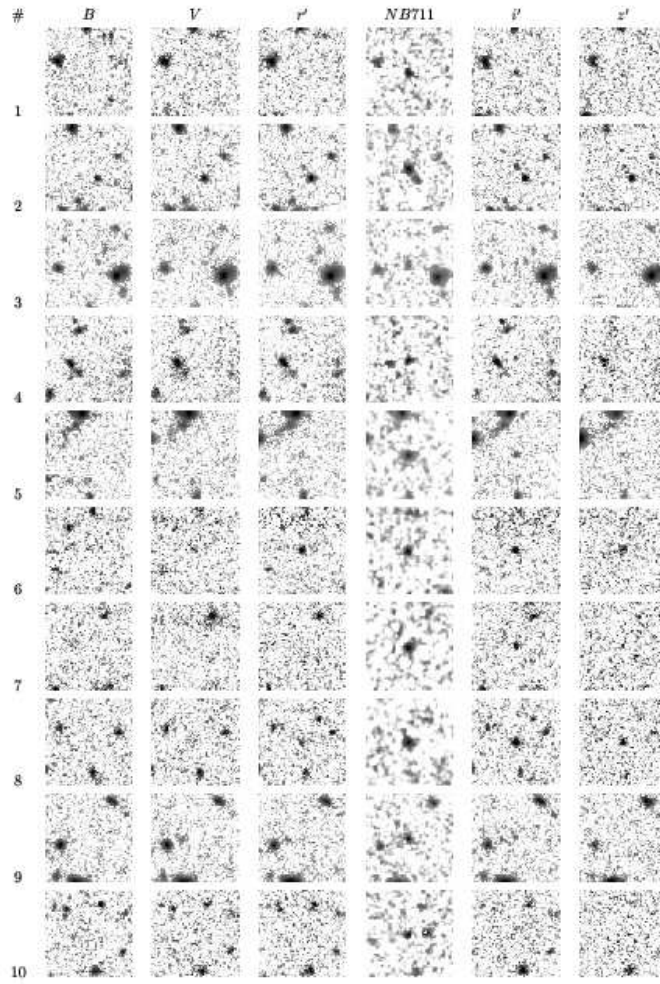


FIG. 4.— Broad-band and NB711 images of our LAE candidates at $z \approx 4.9$. Each box is $12''$ on a side (north is up and east is left).

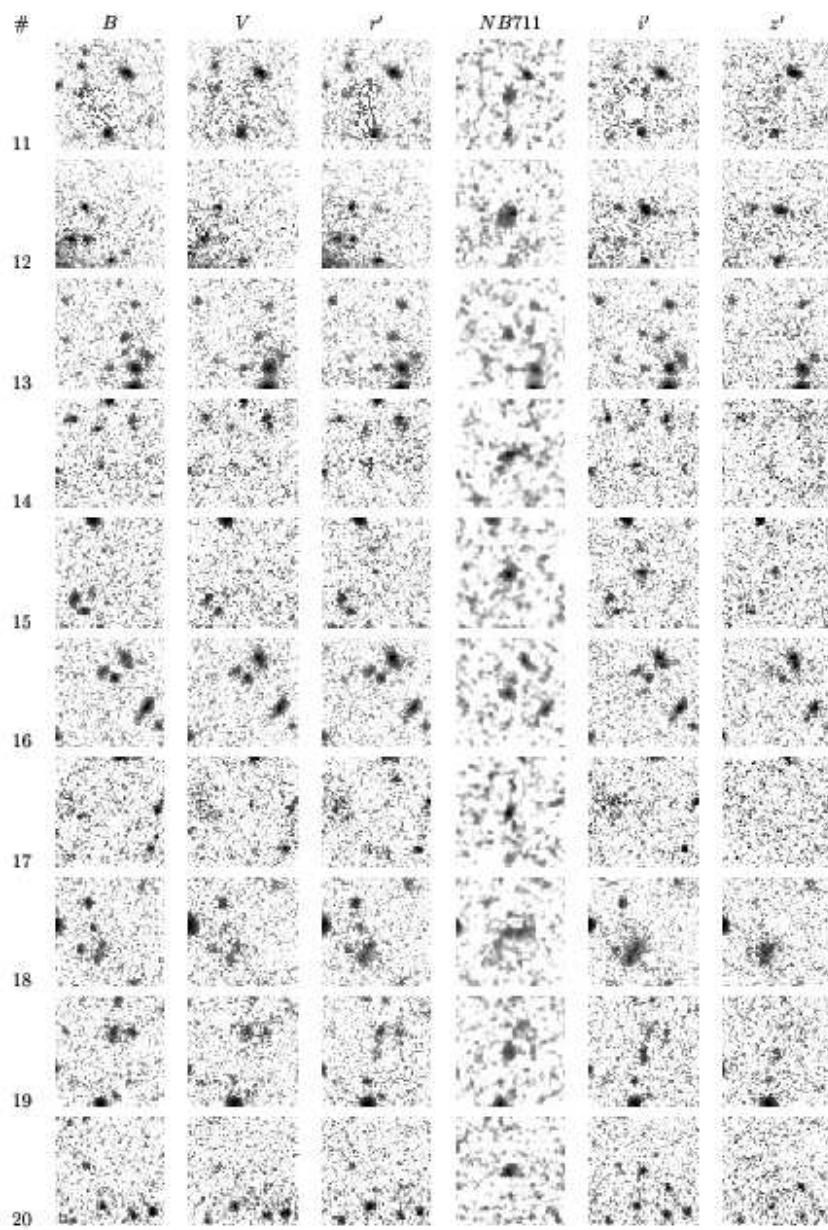


Fig. 4b. — continued.

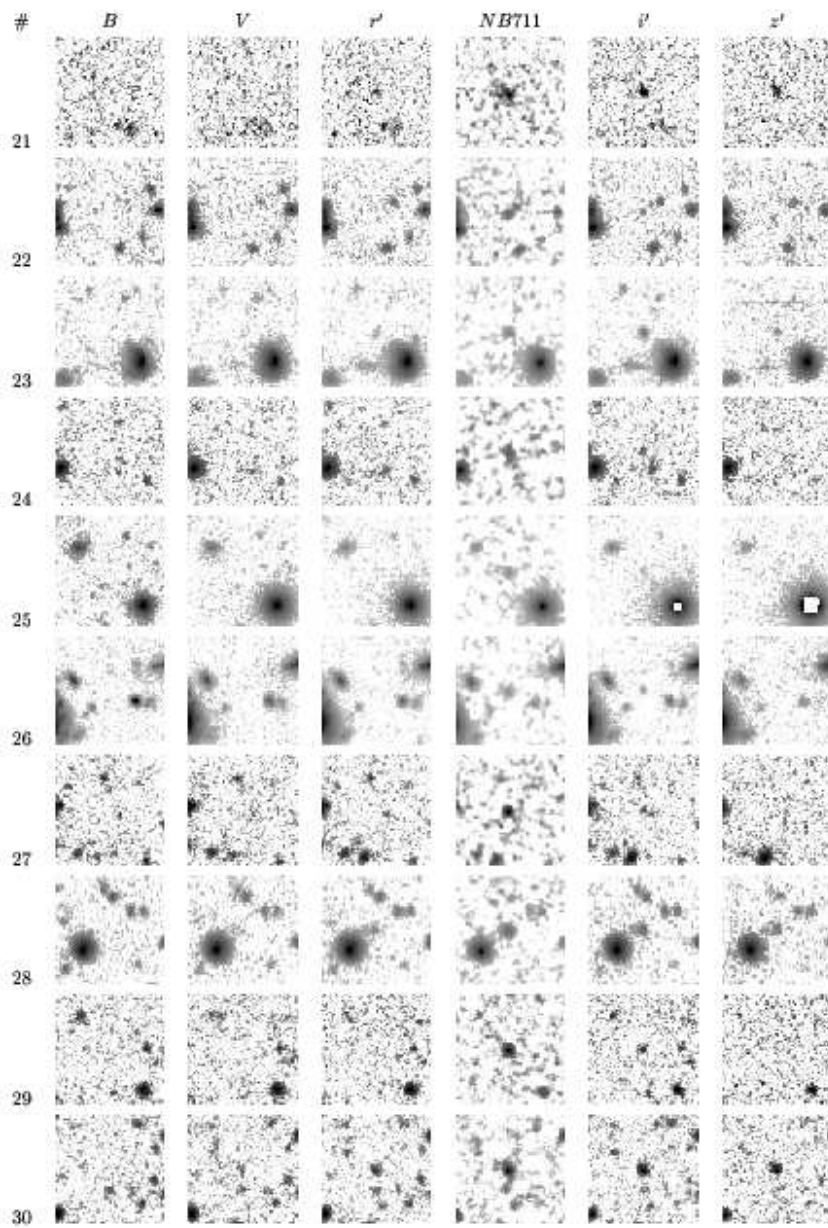


Fig. 4c. — continued.

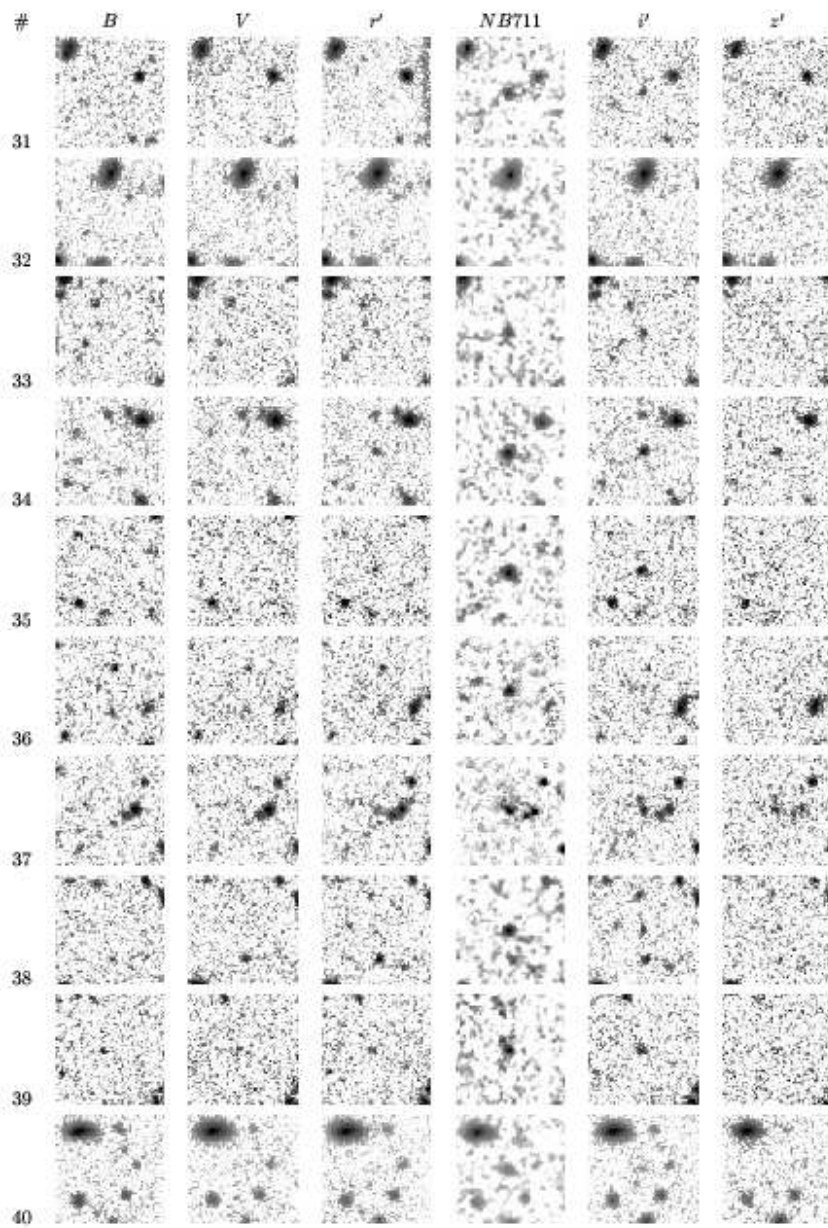


Fig. 4d. — continued.

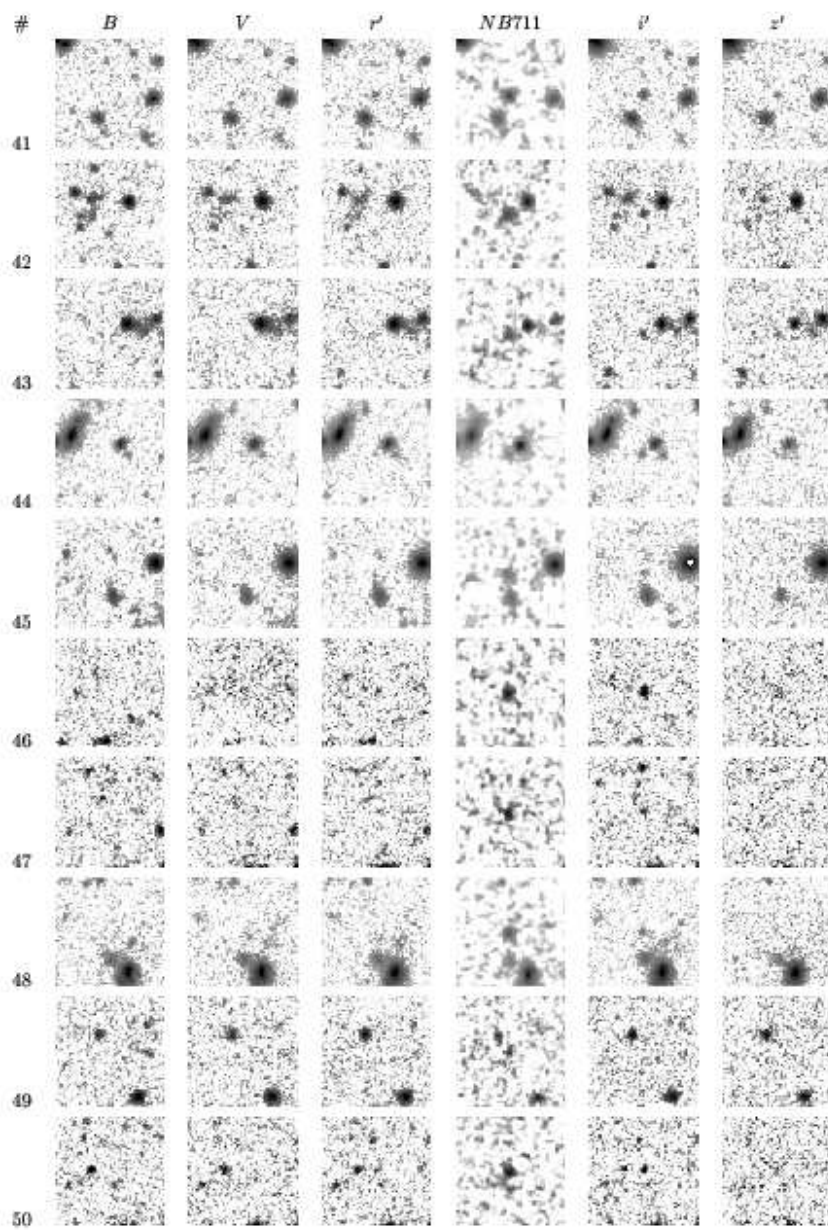


Fig. 4e. — continued.

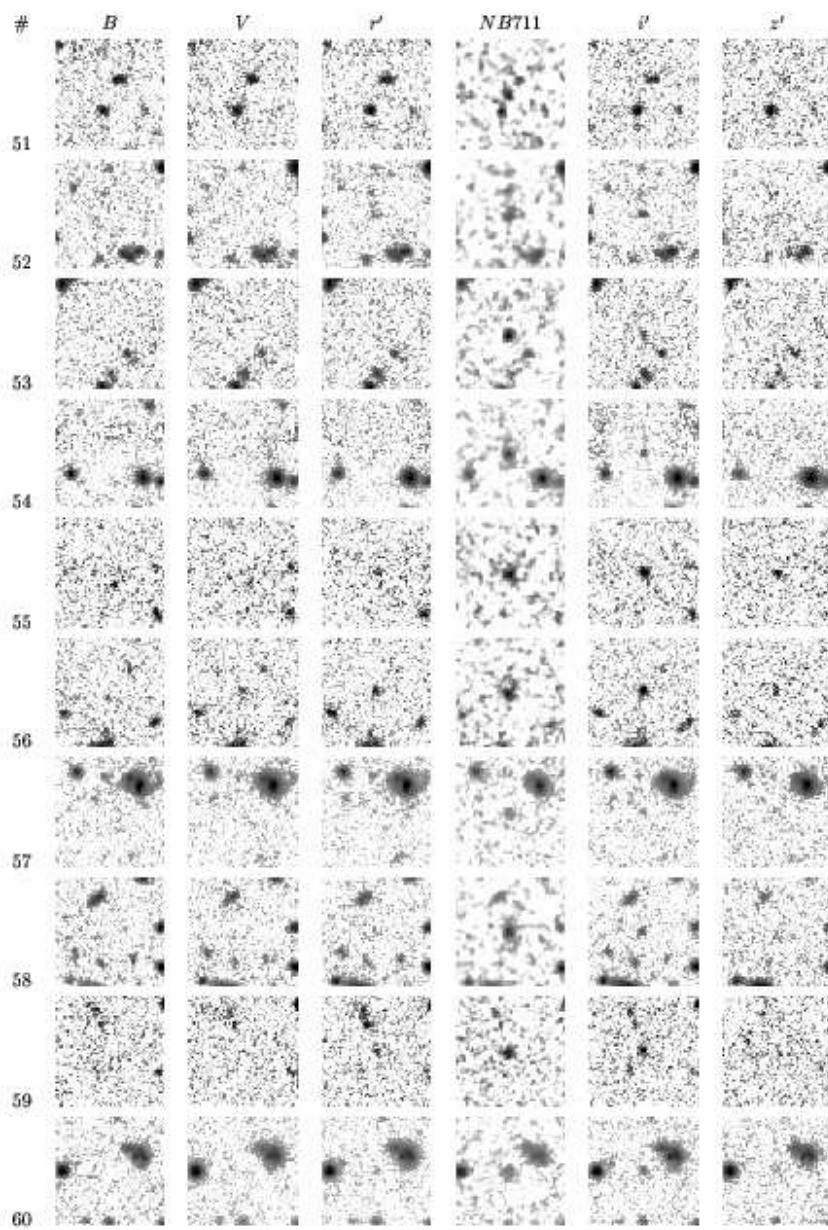


Fig. 4f. — continued.

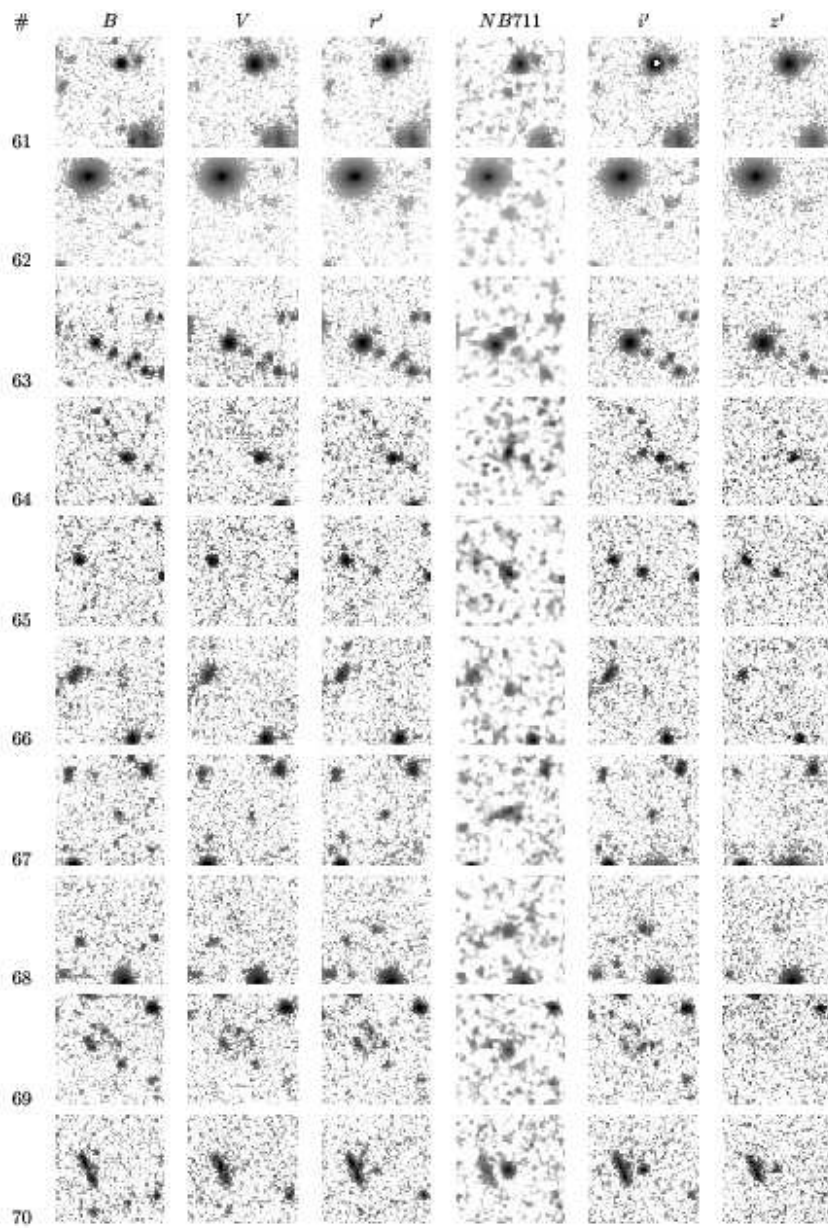


Fig. 4g. — continued.

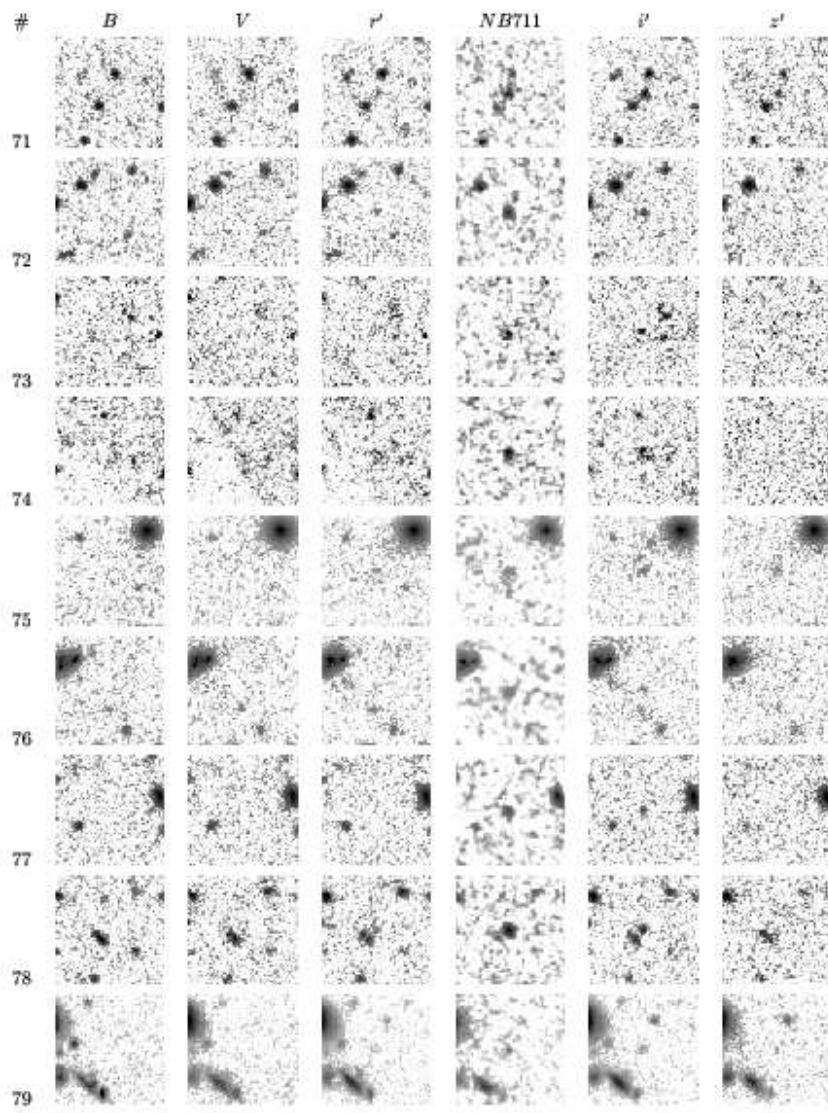


Fig. 4h. — continued.

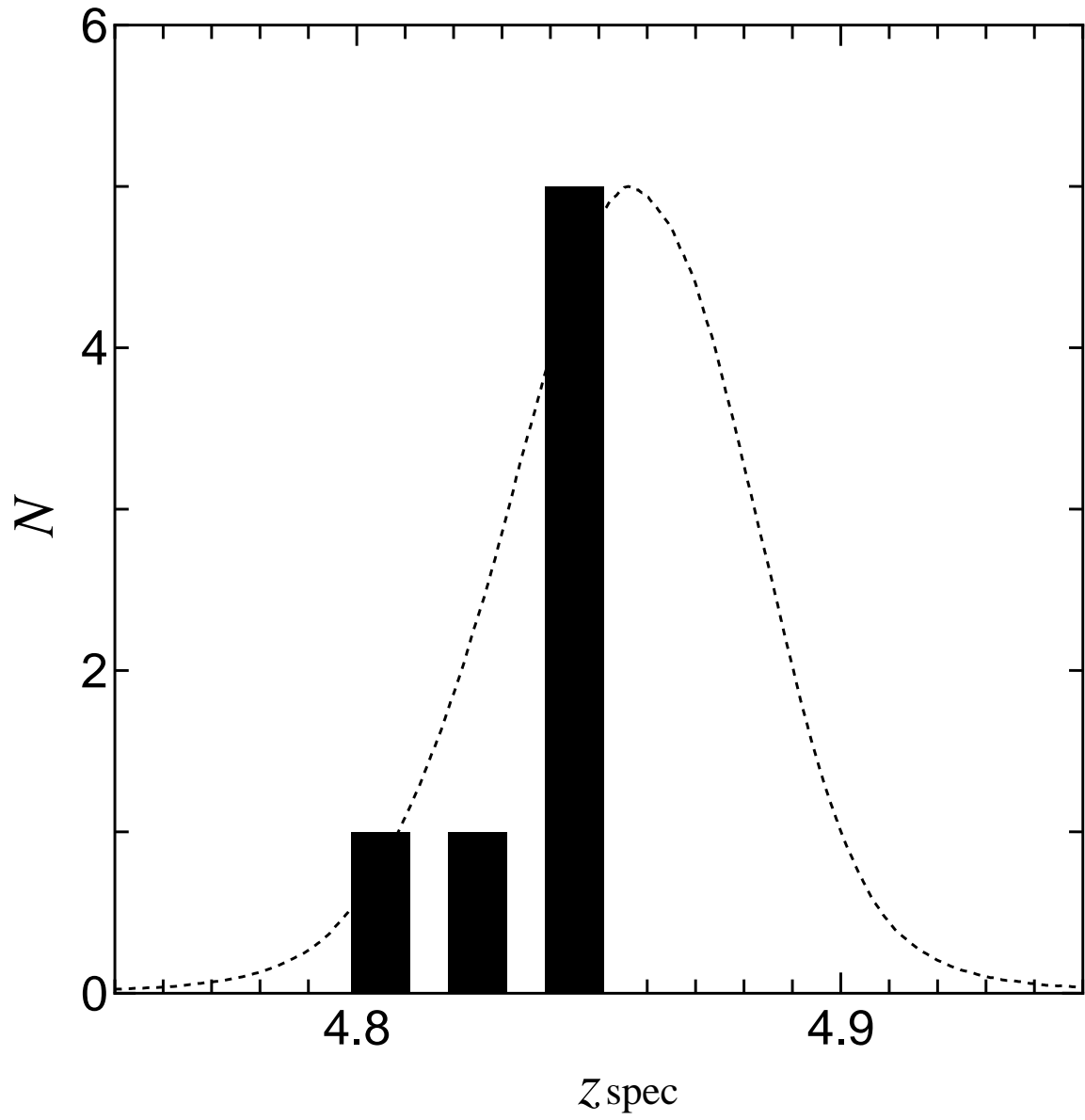


FIG. 5.— Spectroscopic redshift distribution of our LAE sample (7 LAEs). The dotted line shows the response function of the *NB711* band.

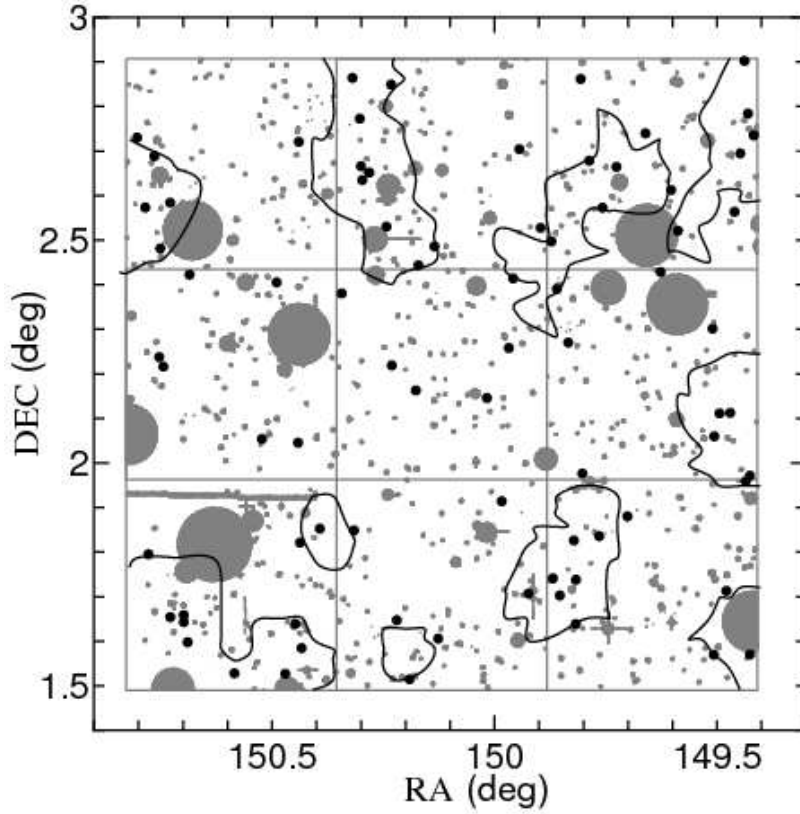


FIG. 6.— Spatial distributions of LAEs (black filled circles). The shaded regions show the areas masked out for the detection. The contours show the local surface density of the LAEs, drawn at the level twice as high as the average over the field, 43 deg^{-2} .

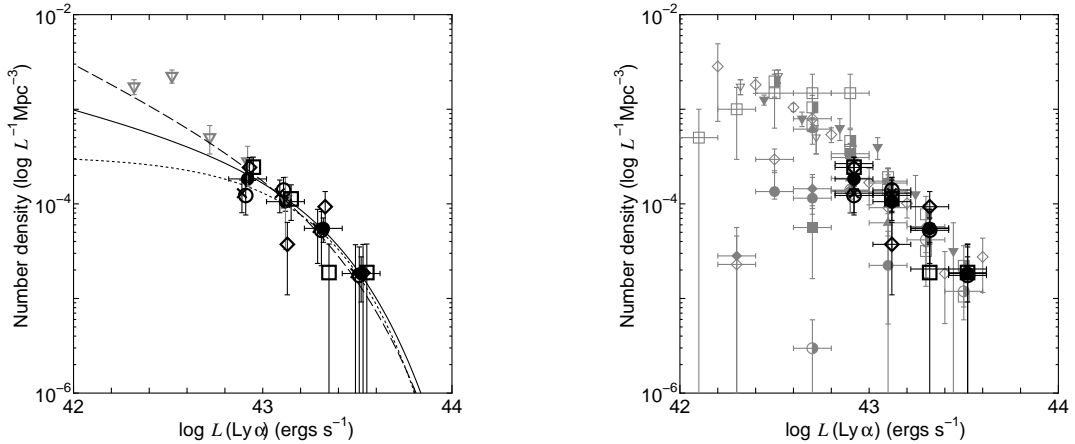


FIG. 7.— Left: The $\text{Ly}\alpha$ LF of our LAE sample (black symbols). The $\text{Ly}\alpha$ LF for the whole sample is shown with filled circles. The dotted, solid and dashed lines show the best-fit Schechter functions for the whole sample for $\alpha = -1, -1.5$ and -2 , respectively. The $\text{Ly}\alpha$ LFs for different quadrants are shown with boxes, diamonds, circles, and crosses for the NE, NW, SW, and SE subfield, respectively. For comparison, the $\text{Ly}\alpha$ LF derived by Ouchi et al. (2003) is shown with inverse triangles. Right: Same as the left panel, compared with other surveys (gray symbols): for LAEs at $z \sim 3.1$ (Ouchi et al. 2008 = circles), $z \sim 3.4$ (Cowie & Hu 1998 = boxes), $z \sim 3.7$ (Ouchi et al. 2008 = triangles), $z \sim 4.9$ (Ouchi et al. 2003 = inverse triangles), $z \sim 5.7$ (Rhoads & Malhotra 2001 = filled circles; Ajiki et al. 2003 = filled boxes; Hu et al. 2004 = filled diamonds; Ajiki et al. 2006 = filled triangles; Shimasaku et al. 2006 = filled inverse triangles; Murayama et al. 2007 = half-filled circles; Ouchi et al. 2008 = half-filled boxes), and $z \sim 6.6$ (Taniguchi et al. 2005 = diamonds).

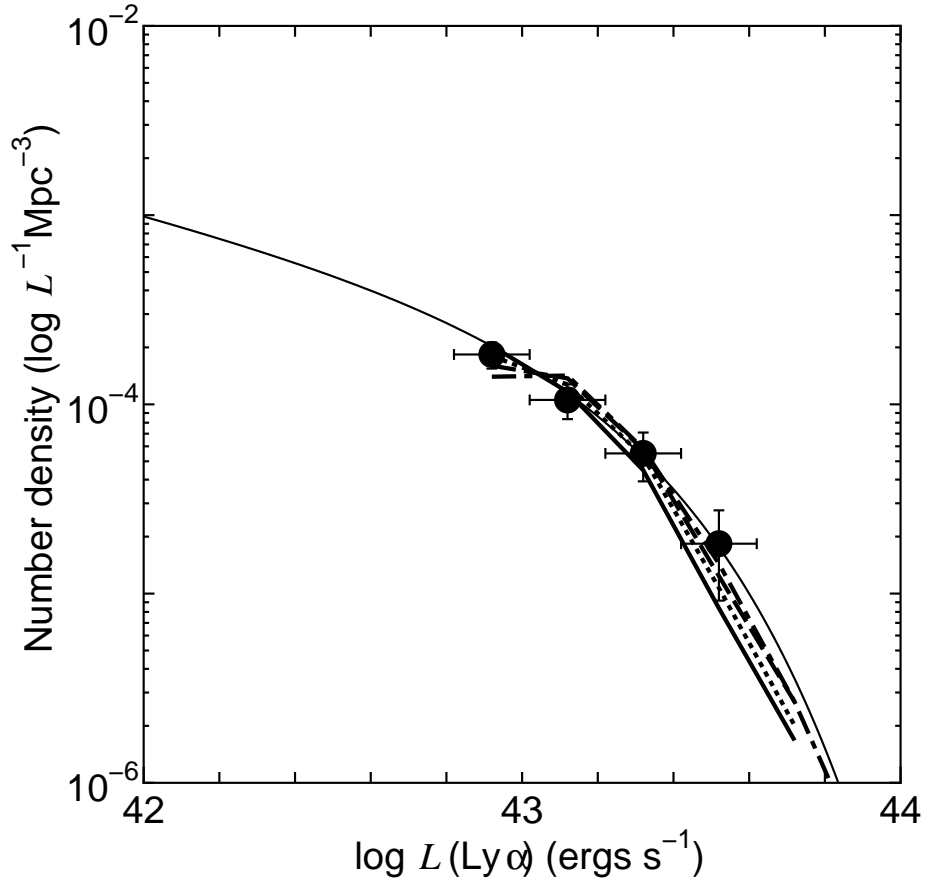


FIG. 8.— Results of our Monte Carlo simulations for $\alpha = -1.5$. The derived Ly α luminosity functions are shown as thick solid line, thick dotted line, thick dashed line, thick dash-dotted line for the case of $\sigma_{EW} = 50, 100, 200, \& 400 \text{ \AA}$, respectively. These luminosity functions are similar to the input Schechter function (thin solid line).

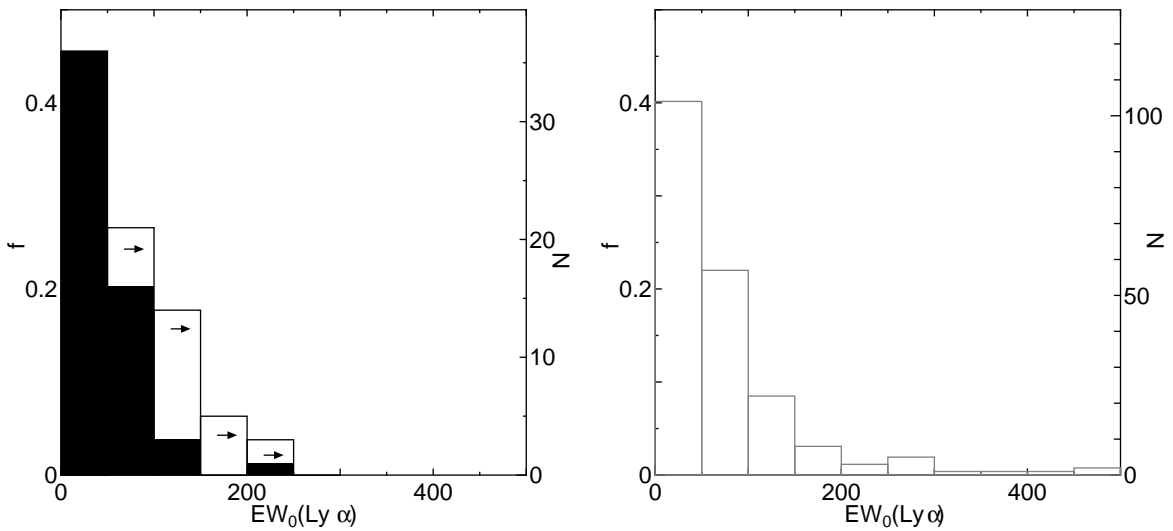


FIG. 9.— Top: Distribution of the rest-frame Ly α equivalent widths. Filled bars show the LAEs with the continuum detected above 1σ . Open bars show the LAEs with no continuum detection. Bottom: Distribution of the rest-frame Ly α equivalent widths of the LAEs at $z \sim 3.1$ obtained by Gronwall et al. (2008).

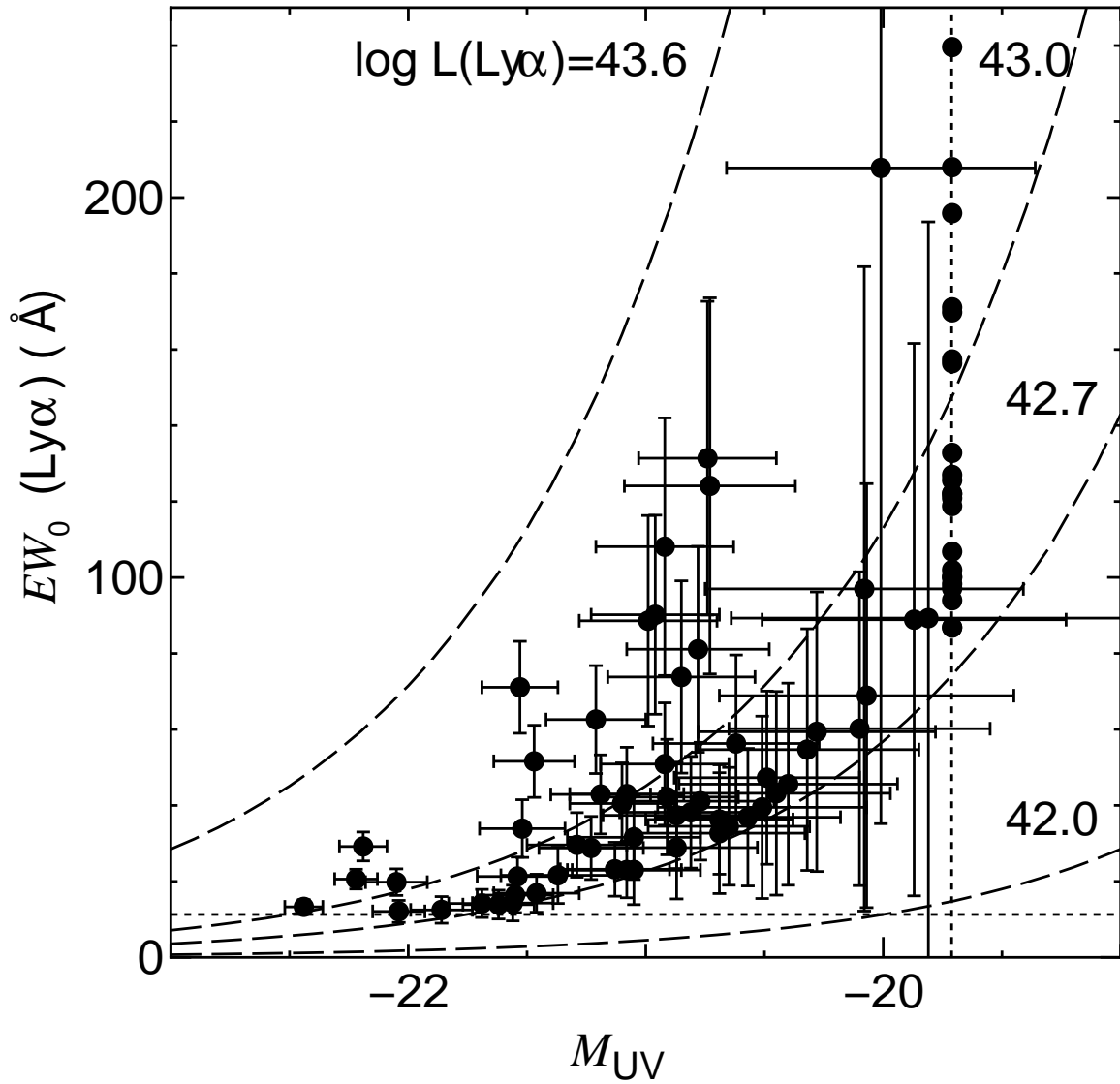


FIG. 10.— Rest-frame EWs of Ly α lines vs. absolute magnitude at rest-frame 1540 \AA for our sample of LAEs at $z \sim 4.9$. Dashed lines show loci of the constant Ly α luminosities for $\log L(\text{Ly}\alpha) = 43.6$, 43.0 and 42.0, where $L(\text{Ly}\alpha)$ is in units of ergs s^{-1} . Dotted line corresponds to $M_{UV} = -19.71$ which is the rest-UV absolute magnitude corresponding to the z' -band limiting magnitude (1σ).

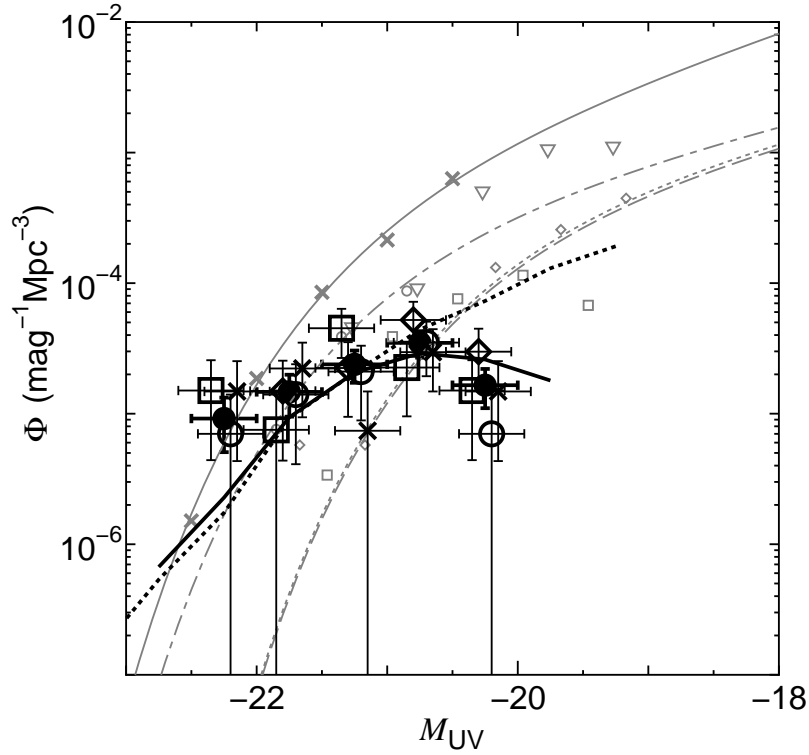


FIG. 11.— The rest-frame UV LF of our LAE sample (black symbols). The UV LF for our whole sample is shown with filled circles. The UV LFs for different quadrants of the COSMOS field are shown with black boxes, black diamonds, black circles, and black crosses for the NE, NW, SW, and SE field, respectively. The results of our Monte Carlo simulation for $\alpha = -1.5$ and $\sigma_{EW} = 100\text{\AA}$ are overlaid: a dotted line show the input UV LF with $EW_0(\text{Ly}\alpha) > 13\text{\AA}$ and a solid line show the output UV LF. For comparison, we show UV LFs from the previous surveys (gray symbols): LAEs at $z \sim 4.9$ (inverse triangles: Ouchi et al. 2003), LBGs at $z \sim 5$ (crosses and solid line: Yoshida et al. 2006), LAEs at $z = 3.1$ (open diamonds and dotted line: Ouchi et al. 2008), $z = 3.7$ (open boxes and dashed line: Ouchi et al. 2008), and $z = 5.7$ (open circle and dot-dash line: Ouchi et al. 2008).

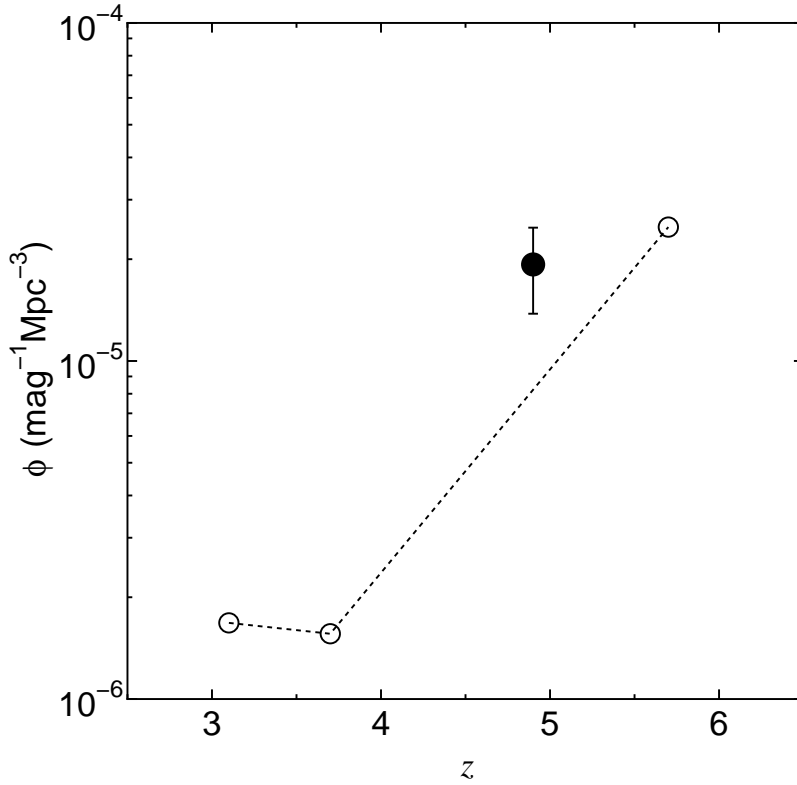


FIG. 12.— Number density of LAEs at $M_{UV} = -21.5$ as a function of z . Our data point is shown with filled circles with a error bar. Open circles show the number densities derived by Ouchi et al. (2008).

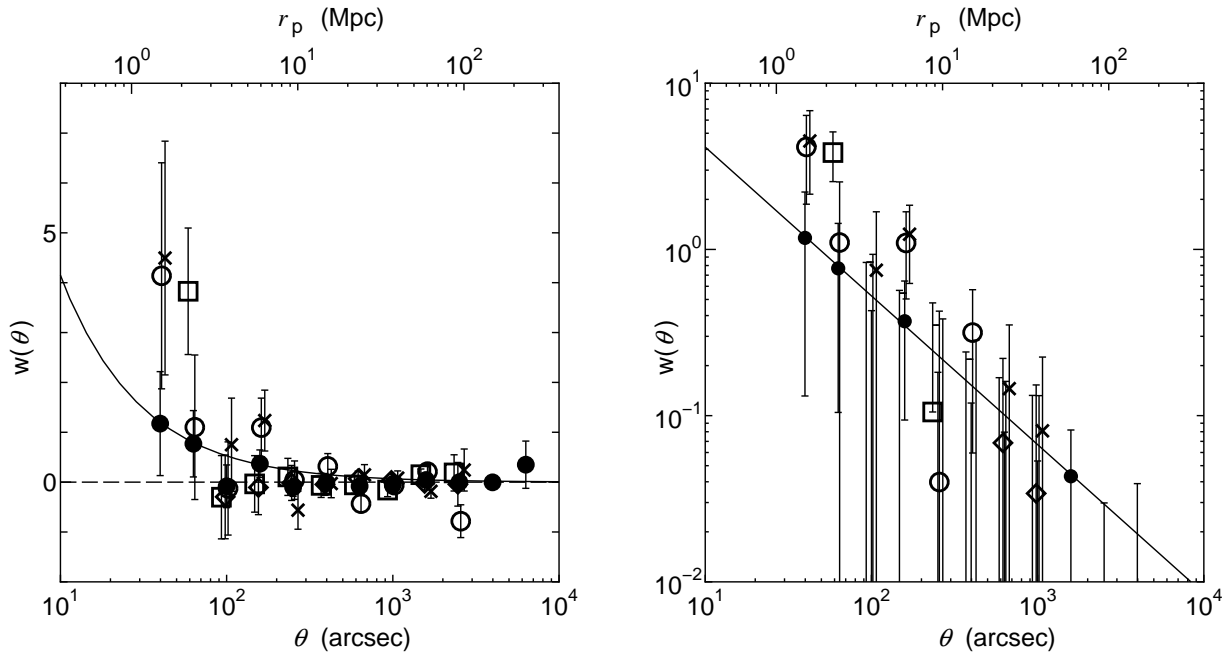


FIG. 13.— Left: Angular two-point correlation function (ACF) of our LAE sample. Filled circles show the ACF for the whole sample. The ACF for different quadrants are shown with boxes, diamonds, circles, and crossed for the NE, NW, SW and SE subfield, respectively. Right: Same as the left panel with $w(\theta)$ shown in logarithmic scale.